Diversity of sharp-wave–ripple LFP signatures reveals differentiated brain-wide dynamical events

Juan F. Ramirez-Villegas[a,b], Nikos K. Logothetis[a,c,1], and Michel Besserve[a,d,1]

[a]Department of Physiology of Cognitive Processes, Max Planck Institute for Biological Cybernetics, 72076 Tübingen, Germany; [b]Graduate School of Neural and Behavioral Sciences, International Max Planck Research School, Eberhard-Karls University of Tübingen, 72074 Tübingen, Germany; [c]Centre for Imaging Sciences, Biomedical Imaging Institute, The University of Manchester, Manchester M13 9PT, United Kingdom; and [d]Department of Empirical Inference, Max Planck Institute for Intelligent Systems, 72076 Tübingen, Germany

Contributed by Nikos K. Logothetis, September 21, 2015 (sent for review May 21, 2015)

Sharp-wave–ripple (SPW-R) complexes are believed to mediate memory reactivation, transfer, and consolidation. However, their underlying neuronal dynamics at multiple scales remains poorly understood. Using concurrent hippocampal local field potential (LFP) recordings and functional MRI (fMRI), we study local changes in neuronal activity during SPW-R episodes and their brain-wide correlates. Analysis of the temporal alignment between SPW and ripple components reveals well-differentiated SPW-R subtypes in the CA1 LFP. SPW-R–triggered fMRI maps show that ripples aligned to the positive peak of their SPWs have enhanced neocortical metabolic up-regulation. In contrast, ripples occurring at the trough of their SPWs relate to weaker neocortical up-regulation and absent subcortical down-regulation, indicating differentiated involvement of neuromodulatory pathways in the ripple phenomenon mediated by long-range interactions. To our knowledge, this study provides the first evidence for the existence of SPW-R subtypes with differentiated CA1 activity and metabolic correlates in related brain areas, possibly serving different memory functions.

hippocampus | memory | in vivo electrophysiology | fMRI | local field potential

Memory processes require mechanisms for large-scale integration of neuronal activity, in which information processing is precisely coordinated at multiple scales. A prominent example of such phenomenon is the replay of specific sequences of action potentials of hippocampal and neocortical neurons, reflecting previous experiences during wakefulness (1–7). Sharp-wave–ripple (SPW-R) complexes observed in the hippocampal CA1 local field potential (LFP) mark the reactivation of these sequences by the simultaneous occurrence of two distinct but related phenomena: a strong LFP deflection, known as sharp wave (SPW), and a high-frequency oscillation known as ripple (8, 9). SPW-R episodes are thought to reflect brain-wide processes mediating memory consolidation (10–13). However, the large-scale cooperative mechanisms associated to these episodes and their relationship to the observed SPW-R electrical signature remain largely unknown. Investigating this relationship is critical for understanding memory processes at a system level and may provide new insights into the mechanisms of pathological fast ripples observed during epilepsy (14).

Although they were initially thought to occur during slow-wave sleep and quiescence periods, later on SPW-R and sequence replay were also observed during or shortly after active behavior (15–17). Moreover, many SPW-Rs occur at path choice points (18, 19), which are also locations where vicarious trial and error are reported (20). Thus, reactivation of memory sequences during SPW-Rs could provide a convenient mechanism not only for consolidation of long-term memory (4) but also for quickly recalling memories during awake state, serving various cognitive functions (21). The generation of SPW-R complexes in these various contexts likely involves brain-wide network mechanisms, and as a consequence, SPW-R–related brain dynamics may vary, reflecting different types of interactions with cortical and subcortical systems. These interactions may in turn affect the underlying dynamics of hippocampal circuits, thus modifying the observed SPW-R–associated functional activity at multiple scales.

In this work, we investigate how the LFP signature of SPW-R events varies during ongoing activity at a given CA1 recording site, and whether these variations reflect differences in the coordination of neural activity at multiple scales, possibly related to different functions. We test our hypothesis by studying the SPW-R correlates at mesoscopic and macroscopic scales. Specifically, using multisite hippocampal LFP recordings and functional MRI (fMRI) in anesthetized rhesus monkeys (*Macaca mulatta*), we examine the spatiotemporal properties of SPW-R complexes with a multivariate clustering approach. This approach revealed that recorded multisite SPW-R LFP activity can be classified in four subtypes differing in the temporal SPW-to-ripple coupling and low-frequency SPW pattern. On the one hand, SPW-R–triggered fMRI statistical maps suggest that ripples synchronized to the positive peak of their SPWs mark enhanced neocortical activations. On the other hand, ripples occurring at the trough of their SPWs reveal weak or absent down-regulation in subcortical structures, especially in two neuromodulatory structures: dorsal raphe nucleus and locus coeruleus. Altogether, our results show that hippocampal episodes displaying specific SPW temporal patterns and distinct couplings between SPWs and ripples may instantiate cortico- and subcortico-hippocampal interactions of different nature, possibly associated with specific memory-related functions.

Significance

Sharp-wave–ripple (SPW-R) episodes observed in the electrical activity of mammalian hippocampus are traditionally associated to memory consolidation during sleep but have been recently observed during active behavior. Their involvement in various cognitive functions suggests the existence of SPW-R subtypes engaged in distinct neuronal activity patterns at multiple scales. We use concurrent electrophysiological and functional MRI (fMRI) recordings in macaque monkeys to investigate this hypothesis. We discover several subtypes of SPW-R with distinct electrophysiological properties. Importantly, fMRI recordings reveal differences between the large-scale signatures of SPW-R subtypes, indicating differentiated interactions with neocortex, and contributions of neuromodulatory pathways to the SPW-R phenomenon. Understanding the detailed properties of hippocampal SPW-Rs at multiple scales will provide new insights on the function of memory systems.

Author contributions: M.B. designed research; J.F.R.-V. performed research; J.F.R.-V., N.K.L., and M.B. contributed new reagents/analytic tools; J.F.R.-V. analyzed data; and J.F.R.-V. and M.B. wrote the paper.

The authors declare no conflict of interest.

Freely available online through the PNAS open access option.

[1]To whom correspondence may be addressed. Email: michel.besserve@tuebingen.mpg.de or nikos.logothetis@tuebingen.mpg.de.

This article contains supporting information online at www.pnas.org/lookup/suppl/doi:10.1073/pnas.1518257112/-/DCSupplemental.

Results

Four Subtypes of SPW-R Complexes. To study the variability of SPW-R complexes, we analyzed extracellular recordings and characterized the temporal and frequency profile of LFPs of the macaque hippocampus. Multicontact recording electrodes were positioned in CA1 on the basis of high-resolution structural MRI scans and on-line tracking of stereotypical hippocampal neuronal response profiles (see *Materials and Methods* for details). Fig. 1 depicts a schematic representation of the recording configuration and typical electrode penetration (Fig. 1*A*), together with an example of a typical SPW-R complex signature across multiple electrode tips (Fig. 1 *B* and *C*). SPW-R amplitude, duration (~100 ms) (Fig. 1*B*), current source density (CSD) profile (Fig. 1*D*), and spectrogram (Fig. 1*E*) are consistent with previous studies in macaque monkeys (22). To check the stability of the level of anesthesia, we monitored the power of hippocampal LFP in the theta frequency band (4–8 Hz) (23). Each experiment of a given session was divided into two blocks (5 min each). The distribution of theta power in these two blocks was assessed by randomly choosing time intervals of 1 min (for a total of 50 time intervals) within the block and computing its theta power using Morlet-wavelet spectrograms (see *Materials and Methods*). Our analysis revealed no significant differences between the first block and second block of each experiment ($n = 242$ experiments; $P > 0.69$, paired-samples permutation t test). Theta activity was thus stable across experiments of single-recording sessions, reflecting no putative fluctuations on the anesthesia levels (Fig. S1 *A* and *B*).

To study the dynamics of SPW-Rs, we have initially identified candidate events using the process described in ref. 24, coupled with several refinements. Briefly, oscillatory events were initially detected as peaks in the envelope of the broadband LFP (10–250 Hz). Candidate events were clustered on the basis of their spectral signatures, and only events exhibiting increases in their spectra above 80 Hz were identified as ripples. Detection of ripples was further refined by quantifying the Z-scored power in the ripple frequency band (80–180 Hz) and ripple localization in time. Only events satisfying stringent localization and power profile criteria were taken into account for further processing steps (see full procedure in *SI Section A*).

To quantify the variability in hippocampal LFP during SPW-R events, we first compared their spatiotemporal signature. We asked whether this variability supported the existence of well-differentiated SPW-R event types, possibly reflecting distinct microcircuit dynamics and functional roles. As a preliminary step, we first aligned perievent waveforms with respect to the averaged ripple power peak across recording sites. We next used a two-step procedure to cluster the detected and aligned SPW-R events as illustrated in Fig. S2. The cluster analysis procedure was performed for each experimental session separately. First, we grouped the spatiotemporal SPW-R series into 200 representative signals using a growing neural gas (GNG) algorithm (25). Each representative signal is the average of a group of raw perievent signals with similar time courses (Fig. S2 *A* and *B*). It is worth noting that GNG does not extract particular features of the signals but represents them solely based on their corresponding time courses in an unsupervised manner. In the second step (Fig. S2*C*), we clustered these representative signals based on their cosine similarity using the normalized cuts algorithm (26) (see *SI Section A* for details).

We applied this two-step algorithm to 12 experimental sessions (a total of ~11,000 detected SPW-R complexes). The results of the clustering procedure were consistent across all experimental sessions and animals, and did not vary significantly due to recording channel selection (the algorithm was amenable to one or multiple recording channels). However, it was difficult to determine whether SPW-R complexes were truly clustered or they only existed as part of some continuum. To address this question, we devised two procedures: clustering quality analysis, and cluster consistency analysis (see *SI Section A* for methodological details, and Fig. S3). The first analysis revealed that the population of SPW-R complexes in the CA1 field is best represented by four LFP signatures. Furthermore, the second procedure revealed that clustering consistency across experimental sessions was significantly higher than chance ($P < 10^{-6}$, t test; mean value with 95% confidence interval for clustering consistency, 74.17% ± 1.63%).

Fig. 2*A* depicts the SPW-R LFP grand averages of the resulting clusters ($n = 12$ experimental sessions, 4 animals), showing that ripple oscillations may follow (subtype 1), precede (subtype 2), or be located at the peak of dendritic depolarization (subtype 3). Additionally, ripples may be deprived from a clear SPW depolarization signature (subtype 4). For brevity, we refer to ripple oscillations located near the peak of the SPW (subtypes 2 and 3) as "classical" (SPW-R patterns with the strongest visual resemblance to those first reported in ref. 22). The remaining SPW-Rs (subtypes 1 and 4) will be referred to as "nonclassical." In correspondence with each SPW-R subtype, typical raw signal traces (0.5–300 Hz) are illustrated in Fig. 2*B* (*Top*) (monkey *i11*), together with their SPW (0–20 Hz) and ripple (80–180 Hz) filtered traces (Fig. 2*B*, *Top* and *Middle*, respectively), a colored dotted line shows the SD threshold for the event in the ripple band. Finally, single-event (broadband) Z-scored Morlet-wavelet spectrograms for every example event are given in Fig. 2*B* (*Bottom*), displaying significant and localized ripple-band power

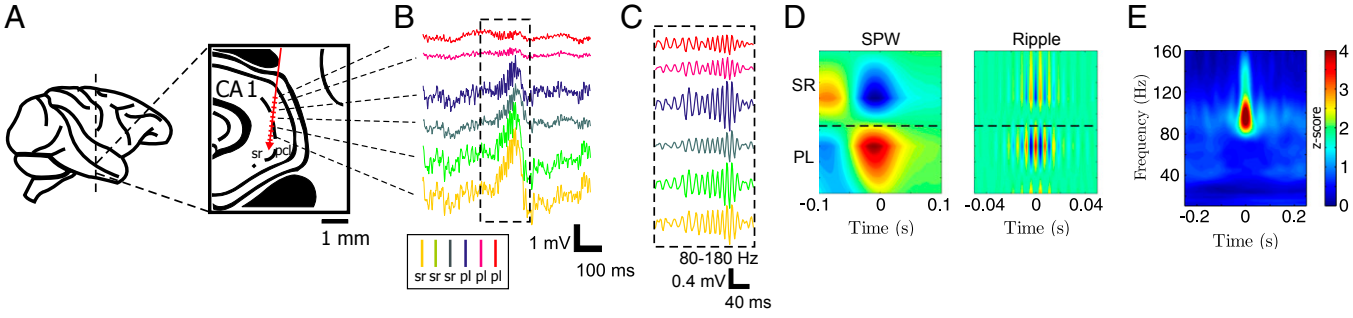

Fig. 1. Electrode position, recordings in the hippocampus, and SPW-Rs. (*A*) Schematic representation of our hippocampal recordings. The diagram of the electrode position is superimposed on an *Inset* of the MRI histology atlas (49) indicating the approximate thickness of the pyramidal cell layer in the CA1 field. (*B*) Raw multisite LFP traces (0.5–250 Hz). Labels indicate the site targeted by each electrode tip: "sr" for stratum radiatum, "pl" for pyramidal layer. (*C*) LFP traces depicted in *B* filtered in the ripple band (80–180 Hz). (*D*) Averaged current source density (CSD) maps (50) for SPW (*Left*) and ripple (*Right*) for a typical experimental session ($n = 1,020$, monkey *i11*). In the CSD plots, warm colors (red) indicate sources, whereas cold colors (blue) indicate sinks. (*E*) Averaged ripple-triggered Morlet-wavelet spectrogram for a typical recording session ($n = 1,020$, monkey *i11*).

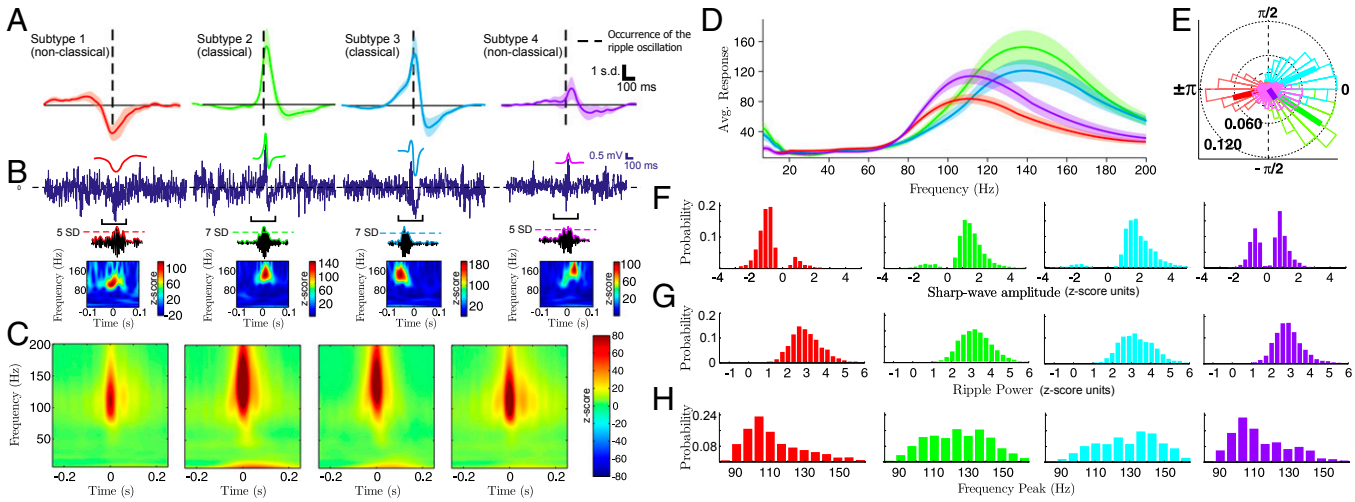

Fig. 2. Classification of SPW-R complexes across 12 experimental sessions in anesthetized macaque monkeys. (*A*) Grand averages of ripple power-triggered SPW-R field potential signatures, from one representative stratum radiatum recording site. Occurrence of the ripple oscillation is marked by dashed lines. Shaded areas indicate SEM. (*B*) Representative single-trial events for each subtype. (*Top*) SPW and related raw signals of each event subtype (monkey *i11*). Note that shapes correspond to the average patterns presented in *A*. (*Middle*) Filtered, *Z*-scored LFP in the ripple frequency range (80–180 Hz), illustrating that all SPW-R classes present a significant power increase in this range. Dashed lines indicate ripple amplitude in SD units. (*Bottom*) *Z*-scored single-event spectrogram of the broadband signal presented in the top rows. (*C*) Spectrogram grand averages, in correspondence with each of the SPW-R signatures depicted in *A*. Averages are computed across all recording sites. (*D*) Averaged clusterwise spectra. Shaded areas indicate SEM. (*E*) Phase coupling of the ripple to the SPW of dendritic depolarization for each cluster. Thick lines indicate the circular mean of the phase-coupling values. (*F–H*) Empirical distribution of SPW and ripple subtypes properties. (*F*) SPW amplitude. (*G*) Ripple power. (*H*) Ripple frequency peak. Colors indicate SPW-R subtype.

increases. We found that results were very consistent from one experimental session to another. As additional evidence, Fig. S4 shows results from another anesthetized experimental session (monkey *e10*). As previous results have shown, single-event ripple band traces and spectrograms show that nonclassical ripples appear localized in line with our selection criteria (*Materials and Methods*), and in good agreement with ripple events reported in the literature (9, 27). It is worth noting that each SPW-R subtype occurred concomitantly across all recording sites, displaying little depth-dependent differences. Furthermore, SPW-R episodes usually maintained the same polarity across all channels.

In addition to average waveforms, we asked whether SPW-R subtypes showed differences in the frequency content of peri-event LFP. Population complex Morlet-wavelet spectrograms corresponding to each SPW-R type are depicted in Fig. 2*C* (n = 12 experimental sessions, 4 animals). This time–frequency analysis shows a clearer low-frequency peak for classical SPW-Rs, suggesting they have higher-power sharp waves than nonclassical SPWs. In addition, the spectral profiles at ripple onset extracted from the middle vertical line of each spectrogram (Fig. 2*D*) show that classical ripples have higher frequency peaks [mean values with 95% confidence intervals, 110.56 ± 1.09, 127.14 ± 0.91, 125.35 ± 0.95, and 115.53 ± 0.83, respectively; pairwise bootstrapped Kolmogorov–Smirnov (KS) test, $P < 10^{-6}$, for the difference between frequency peaks, Bonferroni corrected] and spectral power (*SI Section B* and *SI Section C*, and Fig. S5; specifically note that Fig. S5*H* shows a clear bimodal empirical distribution of the ripple frequency peaks) compared with nonclassical ripples.

A characteristic of our results is the different coupling of average SPW waveforms to the ripple onset. To quantify precisely this relationship in individual events, we measured the phase of the sharp wave (0–20 Hz) at each ripple occurrence. The results, grouped by SPW-R subtypes, are shown as polar histograms on Fig. 2*E*. Classical ripple signatures and only one nonclassical signature (subtype 1, depicted in red) presented statistically significant coupling to the sharp wave (mean values with 95% confidence interval, -2.9126 ± 0.060, -0.53 ± 0.034, and 0.548 ± 0.025; $P < 10^{-10}$, permuted KS test). In contrast, the nonsignificant coupling of the last cluster (subtype 4) (mean value with 95% confidence interval, -0.74 ± 0.091; $P > 0.8$, permuted KS test) is attributable to the lack of clear SPW signature. Notably, ripple-to-SPW coupling was statistically different among all SPW-R subtypes ($P < 0.0001$, permuted KS test; see also Fig. S5*E*, where histograms show clear multimodality). In line with this analysis, the empirical distributions illustrated in Fig. 2*F* show mostly positive SPW amplitude distributions for classical SPW-Rs, whereas nonclassical events show negative distribution or distribution around zero. As illustrated by Fig. 2 *G* and *H*, all SPW-R subtypes have their main spectral support in the frequency range of 80–180 Hz and have similar ripple power profiles (Fig. S5). Altogether, these results suggest that SPW-R subtypes are distinct in several ways, likely reflecting a discrete set of modes for the underlying hippocampal dynamics (e.g., mediated by differentiated inputs to CA1), rather than reflecting a continuum of variations of the same phenomenon. Furthermore, these differences observed at local scales are further supported by subsequent analyses on recording sessions from one unanesthetized animal (*SI Section B* and Fig. S6).

Some of the SPW-R patterns described here are in close correspondence with signatures reported in a previous macaque monkey study (22). Our results extend previous observations on the variability of the time course of SPW-R complexes across species (9, 22, 28). In fact, Skaggs et al. (22) suggested that ripple oscillations come before the largest deflection of SPW in macaque monkeys. Here, we demonstrate that SPWs and ripples exhibit a variety of couplings. Moreover, our findings show that SPWs also come in different shapes. In *SI Section B*, we further characterize SPWs and ripples of distinct type. In particular, we report comparable ripple power, and higher ripple peak frequency for classical SPW-Rs with respect to their nonclassical counterparts (see the overall ripple and SPW statistics across experimental sessions in Fig. S5). These differences may be related to changes in neuronal synchrony (recruitment of pyramidal neurons and interneurons) and modifications of the *E–I* balance resulting in a higher neuronal excitability during classical SPW-Rs. Interestingly, we also report that, although subtypes have comparable rates and appear at similar timescales (Fig. S7

A and *B*), classical sharp waves have larger autocorrelation density ($P < 0.01$; t test; $n = 12$ experimental sessions), suggesting larger burstiness for these subtypes (Fig. S7*C* and *SI Section B*), and consistent with previous studies reporting that ripples tend to occur at comparable timescales, in time windows of increased multiunit spiking activity (29). We now investigate the coupling of SPW-R signatures to multiunit spiking activity.

Spike-Field Coherence Reflects Differences in Population Synchrony During SPW-R Subtypes. Ripples are correlated with single-unit and multiunit spiking activity from the CA1 pyramidal layer (9, 27). We asked whether this was the case for the identified SPW-R subtypes. Using the recorded multiunit spiking activity, we computed perievent time histograms (5-ms bins) for each SPW-R subtype across experimental sessions. For such a purpose, we limited our analysis to the electrode tip with the largest ripple oscillation power located in stratum pyramidale (see *SI Section A* for details). Our first analysis revealed a significant increase in spiking activity from baseline (Fig. 3*A*; $n = 12$ experimental sessions) concomitant with the ripple occurrence. Broadly, spiking activity of all SPW-R event types peaked at the same time.

Ripple events have a characteristic phase relationship to the firing of participating units (8). We thus asked whether this relationship was the same for differentiated SPW-R subtypes. We assessed precisely the relationship between multiunit spikes and LFP phase using cross-correlation. For this analysis, the SPW-R signal was bandpass filtered in the ripple range (80–180 Hz), and we used the location of the largest trough of the oscillation as event onset reference for the cross-correlation. We then computed the ripple trough-triggered perievent time histograms (bins of 2 ms; $n = 12$ experimental sessions). Our results not only indicated that neuronal assemblies increase their discharge probability (Fig. 3*A*) during the occurrence of SPW-Rs but also revealed that unit discharges occur preferentially at the negative peaks of the ripple oscillations (ripple trough) (Fig. 3*B*), in agreement with previous studies in rats (8, 9). This finding was consistent across all SPW-R event subtypes, displaying virtually identical cross-correlograms (Fig. 3*B*, *Top*). In addition, the average ripple oscillation signature was almost identical among SPW-R subtypes.

Differences in the relationship between multiunit spikes and LFP across SPW-R subtypes may also span over the entire frequency axis, instead of remaining localized to a particular frequency band (such as the ripple range). Hence we further studied the LFP–spike relationship of SPW-R subtypes using spike-field coherence (SFC) of each SPW-R cluster across all frequencies in the [0–200 Hz] range (30) (see *SI Section A*). We computed this quantity for the four SPW-R signatures independently, across all experimental sessions. SFC group results are shown in Fig. 3*C* for each SPW-R subtype ($n = 12$ experimental sessions). Absolute values reported in Fig. 3*C* reveal coherency peaks both in the ripple and sharp-wave frequency bands. Classical SPW-Rs have the highest coherence values. Furthermore, the ripple-band peak of coherency of nonclassical events was consistently below that of classical SPW-Rs, in agreement with previous analyses (Fig. 2 and Fig. S6).

We further investigated whether spikes had a consistent phase relationship to LFP at different frequencies. Phase-locking values and circular mean phase of the coherence maps are reported in Fig. 3*D*. Consistent with our preliminary analysis, we found that multiunit spikes were phase-locked approximately to the trough of the ripple oscillation (corresponding to a phase of π radians or 180°; Fig. 3*D*, middle map plots; mean phase with 95% circular confidence interval -2.84 ± 0.04 radians or $197.28 \pm 2.29°$ for subtype 2; -2.62 ± 0.02 radians or $209.78 \pm 1.25°$ degrees for subtype 3). However, in our SFC result, this relationship holds more precisely for classical ripples (nonclassical ripples mean phase with 95% circular confidence interval -2.32 ± 0.04 radians or $227.07 \pm 2.29°$; -2.52 ± 0.05 radians or $215.61 \pm 2.86°$; $P < 10^{-3}$, paired Kuiper test for the difference between phase couplings of all ripple subtypes, Bonferroni corrected). This finding most likely reflects different degrees of neuronal population synchrony 50 ms around the occurrence of the ripple oscillation for different types of SPW-R complexes, which may explain the difference between our preliminary results and those with the SFC. Furthermore, this finding also suggests that nonclassical episodes represent the activity of a less synchronous neuronal population, in agreement with results in Fig. 3*C*.

Finally, SFC analysis shows that multiunit spiking activity is significantly locked to the gamma rhythm. A previous study showed that a gamma rhythm is ubiquitous in the SPW-R phenomenon (31). Notably, the results of this study suggest that SWR-related gamma coordinates CA3 and CA1 assemblies, and could coordinate the reactivation of stored memories. It is worth noting that, in the present work, we only selected "pure" ripple events taking into account a signal-to-noise ratio, thus assuring an almost unimodal ripple band power profile (24) (*SI Section C*). To fully account for the possible influence of putative perievent gamma oscillations, we considered all detected events, namely pure and "nonpure" events in two separate groups. In *SI Section C*, we show that detailed examination of SPW-R episode-related gamma oscillations across all detected nonpure events reveal neither new SPW-R LFP signatures nor distinct electrophysiological features compared with pure events (see Fig. S8 *A–D*). Interestingly, we found a transient increase of power over gamma frequencies concomitant with the occurrence of pure, nonpure, and

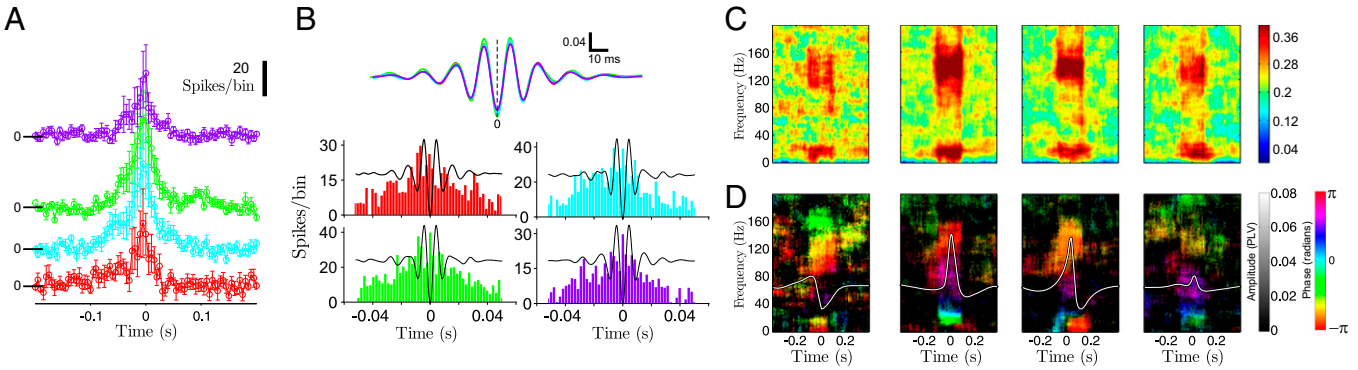

Fig. 3. Relationship between SPW-R complex subtypes and neuronal spiking activity. (*A*) Perievent time histograms of multiunit spiking activity using bins of size 5 ms. Histograms are computed with respect to random point processes of the same rate. (*B*) Cross-correlogram (*Top*) and ripple-trough perievent time histograms (*Bottom*). (*C*) Maps of absolute SFC for each SPW-R subtype defined in Fig. 3. (*D*) Spike-field phase-locking maps corresponding to SFC map displayed in *C*.

all SPW-R subtypes (Fig. S8*E*). These oscillations spread over the slow- and high-gamma range of 25–75 Hz, with a unimodal distribution of instantaneous frequencies peaking at ∼50 Hz (see Fig. S8*C*, *Insets*). We found that individual SPW-R episodes can be predicted—to a certain extent—from this transient increase in gamma power, but not their specific subtype (Fig. S8*F*). Furthermore, in line with our SFC analysis, the relationship between gamma LFP and multiunit spikes displays significant differences in phase-coupling and phase-locking value among SPW-R subtypes, further supporting our hypothesis that these episode subtypes are functionally different (Fig. S8*G*). Importantly, these results demonstrate that our observations are invariant to SPW-R event detection protocols, and most likely reflect the intricate hippocampal dynamics. Furthermore, in line with ref. 31, our data suggest that macaque SPW-Rs are also mediated by a gamma rhythm (see *SI Section C* and *SI Section D* for further discussion).

Brain-Wide Signatures During Distinct SPW-R Episodes. To investigate the differentiated signature of each SPW-R subtype on brain-wide activity, we measured neural event-triggered fMRI (NET-fMRI) for a set of regions of interest (ROIs) (24). The occurrence of each SPW-R complex was used as a reference (trigger) to align and average the time course of the blood oxygenation level-dependent (BOLD) fMRI signal (see *Materials and Methods*). We defined the ROIs according to previously established functional specificity criteria (24). We analyzed the averaged *Z*-scored BOLD maps for each experimental session, across four animals. Because classical SPW-R (subtypes 2 and 3) have virtually identical ripple-triggered fMRI signature, they were averaged together. First, we tracked qualitative differences in brain-wide activations for the three remaining SPW-R subtypes (subtype 1, subtype 2–3, and subtype 4).

As shown in the population analysis across all experimental sessions (n = 12 experimental sessions, 4 monkeys, Fig. 4*A*; see Fig. S9 *A* and *B* for examples in individual animals), the overall NET-fMRI time courses of all subtypes matches previously reported observations: cortical up-regulation and subcortical down-regulation. However, BOLD responses related to classical SPW-Rs exhibit the largest cortical up-regulations and subcortical down-regulations. In agreement with these observations, significant differences between BOLD activations of classical and nonclassical subtypes are observed in both neocortical and subcortical domains (KS test, $P < 0.02$; Fig. 4*B*), with larger effect over subcortical domains in the case of event subtype 1 (Fig. S9*C*).

We found no significant deactivation of subcortical structures associated with SPW-R subtype 1 (t test, Bonferroni-corrected, $P > 0.36$), with very low amplitude or no negative deviation from zero. Interestingly, SPW-R subtype 1 was related to increased neocortical BOLD responses compared with SPW-R subtype 4, the last being associated with weak cortical up-regulation, and subcortical down-regulations qualitatively comparable to that of subtypes 2–3. The grand average NET-fMRI results are shown in Fig. 5*A* for a large number of ROIs. We assessed how subtype 1 and subtype 4 differed from classical SPW-Rs (subtypes 2–3) in each ROI. Because ROI-associated NET-fMRI responses exhibit similar shapes across subtypes, presenting differences mostly in magnitude, we extracted the average NET-fMRI response over the full width at half absolute maximum and compared the magnitude of up- or down-regulation for each ROI across subtypes with univariate statistical tests corrected for multiple comparisons. We found significantly higher up-regulation during classical SPW-Rs than during nonclassical SPW-Rs within the hippocampal formation, and in cortical associative areas (posterior

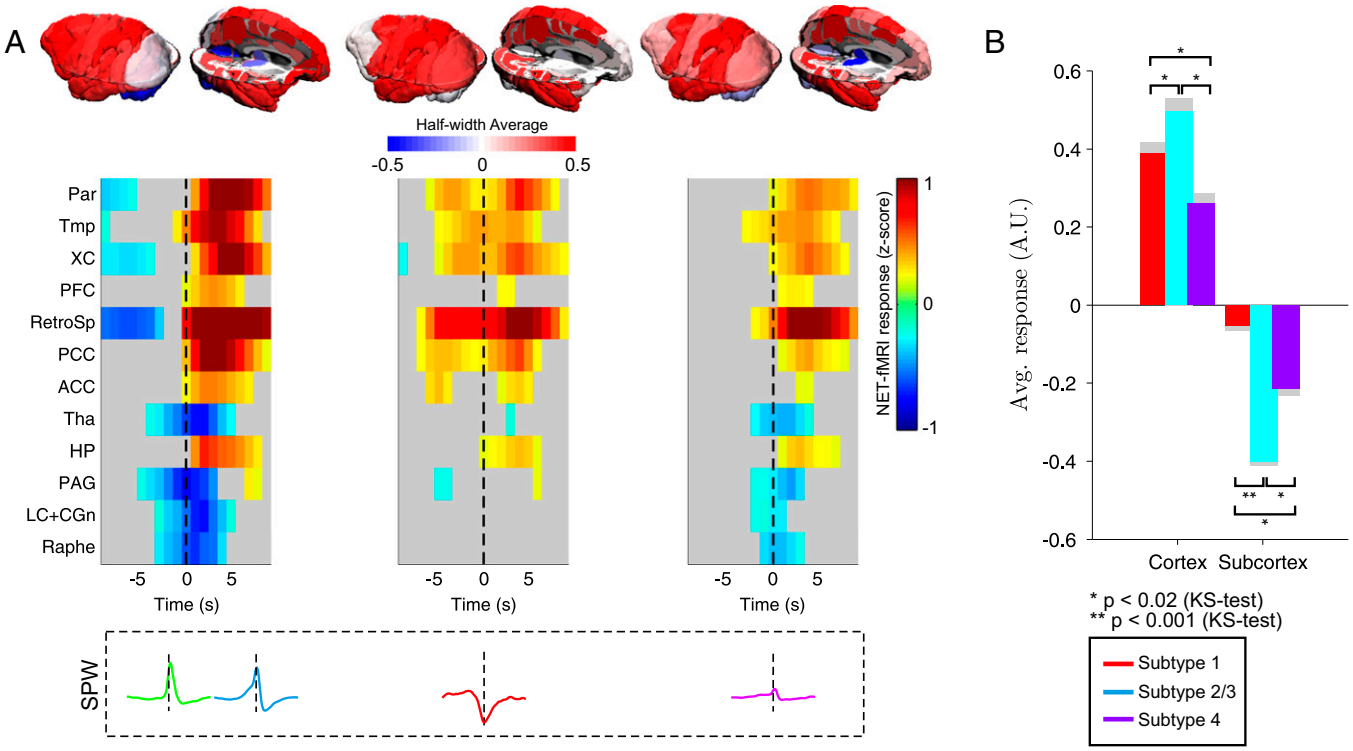

Fig. 4. Ripple-triggered NET-fMRI associated with SPW-R subtypes. (*A*) Absolute averaged BOLD full-width at half absolute maximum, illustrating that significant activation related to subtype 1 occurs almost exclusively for neocortex. Event subtypes 2 and 4 present heterogeneous activations across all brain domains (*Top*). Averaged BOLD time courses show differentiated neocortical activations and subcortical deactivations for distinct event subtypes in *Z*-score units across 12 experimental sessions, 4 animals. The gray regions in the previous plots represent activations below a 0.3-*Z*-score-units threshold to ease visualization (*Bottom*). (*B*) Averaged cortical and subcortical BOLD responses computed using the first singular-value decomposition (SVD) component (Fig. S9).

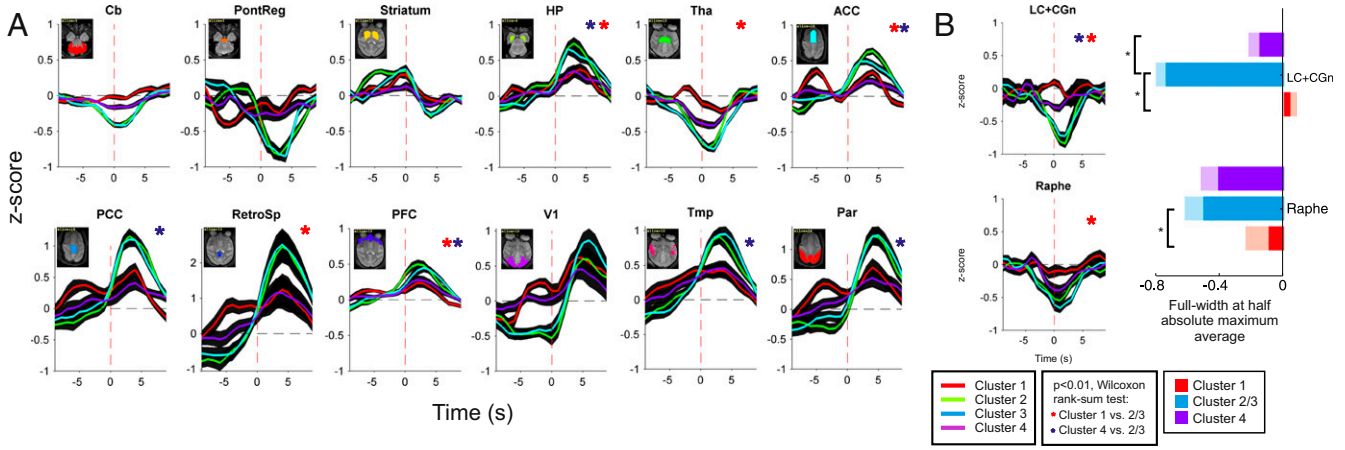

Fig. 5. Population ripple-triggered NET-fMRI time course in ROIs for each SPW-R subtype. (*A*) Average BOLD response show differentiated activations (all experimental sessions) of hippocampus (HP), thalamus (Tha), posterior and anterior cingulate cortices (PCC, ACC), retrosplenial area (RetroSp), and prefrontal (PFC) and parietal (Par) cortical areas (significant differences are indicated by asterisks). Black-shaded areas indicate SEM. (*B*) Average NET-fMRI responses (full width at half-maximum) show differentiated contributions of two neuromodulatory structures, dorsal raphe nucleus (serotonergic) and locus coeruleus (noradrenergic), to the SPW-R phenomenon (Fig. S10).

and anterior cingulate cortex, retrosplenial area, prefrontal, temporal, and parietal cortices) (Fig. 5*A*).

In support of previous analyses, nonclassical SPW-Rs gave rise to differences between subcortical down-regulation profiles. Detailed statistical analysis of all subcortical ROIs showed that differentiated BOLD activations occur in periaqueductal gray (PAG), thalamus, mesencephalon, locus coeruleus (LC), and dorsal raphe nucleus (Fig. S10*B*). The last two areas are neuromodulatory structures known to exert control on the overall brain state, and may influence the emergence of SPW-Rs. Notably, we found that, compared with classical SPW-Rs, subtype 1 (Fig. 5*B*, red curves) was associated with weaker deactivation of LC and raphe [$P < 0.002$, pairwise Wilcoxon rank-sum test, false-discovery rate (FDR) corrected with $q_{FDR} < 0.05$] (Fig. 5*B*, red bars). In contrast, during the occurrence of SPW-R subtype 4, deactivation of the raphe was comparable to that of classical SPW-Rs ($P > 0.1$, Wilcoxon rank-sum test, FDR corrected with $q_{FDR} < 0.05$), but LC down-regulation was significantly weaker ($P < 0.002$, pairwise Wilcoxon rank-sum test, FDR corrected with $q_{FDR} < 0.05$) (Fig. 5*B*, purple bars).

Discussion

In the present study, we identified—for the first time (to the best of our knowledge)—distinct subtypes of in vivo SPW-R patterns in a single recording site, displaying qualitative and quantitative electrophysiological differences. Our procedure reliably clusters the perievent time series into a number of event subtypes; examines their characteristic properties, such as their frequency content, amplitude, and frequency of occurrence; and maps the topology and dynamics of brain-wide metabolic activity at the time of event occurrence.

This approach revealed the existence of four hippocampal SPW-R subtypes with differentiated mesoscopic and brain-wide dynamics. Subtype identification relied on the presence of a SPW pattern in the LFP trace and its shape. The characteristics of SPW patterns and ripple oscillations in the hippocampal CA1 subfield suggested differences in subthreshold activity of the underlying neural populations. Importantly, such differences at the mesoscopic level were complemented by differences in brain-wide signatures mapped with NET-fMRI. Our results demonstrate significant modulation of two brain-wide networks linked to hippocampal-dependent memory functions: one involving associative neocortex, and another one involving subcortical and specifically neuromodulatory structures.

It is unlikely that our results are an effect of fluctuations in the levels of anesthesia (in the case of the four anesthetized animals), because the low-frequency LFP activity over the theta range was stable over time for each experimental session. Furthermore, the occurrences of SPW-R complex subtypes showed no apparent clustering in time for different event types and were comparable to those observed in experimental sessions from one drug-free animal, recorded during quiet wakefulness.

Identification of Four Subtypes of the SPW-R Phenomenon. We have demonstrated that hippocampal LFP dynamical variability during SPW-Rs can be summarized into four typical signatures. Each signature corresponds to a specific relationship between SPWs and ripple oscillations: high-frequency oscillations preceding, following, or coinciding with the peak of the SPW of dendritic depolarization, as well as high-frequency oscillations with no clear SPW signature. Such highly structured variability suggests differentiated underlying neural mechanisms, possibly associated with different memory-related functions.

Some SPW-R subtypes reported in the present work are in agreement with recently reported SPW-R signatures in slice models (32, 33). However, Hofer et al. (32) report only two event classes based on the SPW polarity in CA3. In contrast, Reichinnek et al. (33) have also observed two SPW-R event classes, differing only in SPW amplitude. The discrepancy between previously reported results and ours may be due to the chosen SPW-R detection protocol, solely based on SPW amplitude and visual inspection (33), and also to the limitations inherent to slice models, unable to reproduce the effect of long-range brain interactions.

The observed variability of LFP profiles during ripples suggests a different spatiotemporal repartition of extracellular currents in the CA1 microcircuits, possibly resulting from the differences in the recruitment of—and interactions between—the underlying neuronal subgroups. Indeed, several inhibitory and excitatory subgroups of neurons interact during SPW-R episodes, and their nonhomogenous spatial configuration can affect the spatial distribution of extracellular activity. For instance, Mizuseki et al. (34) report differential involvement of the two CA1 pyramidal sublayers, having distinct phase shifting with respect to the theta rhythm during rapid eye movement (REM) sleep, and they further indicate that REM shifting cells were more strongly associated with SPW-R activity, compared with that of non-REM shifting cells. Whether these two sublayers are differen-

tially involved during SPW-R subtypes and are at the origin of the observed LFP characteristics remains an open question.

Another candidate for modulating the physiological properties of SPW-R is the influence of CA3. In particular, gamma oscillations during SPW-R are assumed to play a central role in coordinating CA3 and CA1 cell assemblies during memory replay (31). We discovered that a gamma rhythm is ubiquitous in all SPW-R subtypes. Specifically, we found a transient increase in gamma power concomitant with the occurrence of SPW-R episodes, and barring the detailed single-unit analysis, we found similar SWR-gamma correlates as those reported in ref. 31. Thus, gamma-related mechanisms mediating CA3–CA1 interactions during SPW-R episodes seem to be independent from the mechanisms generating the SPW-R diversity.

Additional discussion about the possible influence of the recording locations and the local circuits in stratum pyramidale within CA1 in relation to our results can be found in *SI Section D*. Although the above comments discuss modifications of hippocampal neural activity that might explain our LFP observations, we hypothesize that these changes may in turn result from the influence of other brain structures.

SPW-R Subtypes Relate to Differentiated Neuromodulatory Activities. Modulations in amplitude of the BOLD responses in subcortical domains suggest the involvement of two neuromodulatory structures directly connected to hippocampus in the SPW-R phenomenon, namely dorsal raphe nucleus and LC. Due to the transient nature of the examined neuronal events, the lack of clustering of the SPW-R subtypes, and their NET-fMRI correlates, it is likely that our study reflects short-duration "phasic" changes, rather than tonic neuromodulatory effects spanning over 10 s or larger timescales.

A dense noradrenergic and serotonergic innervation is present in the hippocampus proper, exerting modulatory effects in the activity of microcircuits. For instance, LC deactivation is involved in switching cortex and hippocampus to inactive states (35). However, LC neurons exhibit also phasic modes of activity, with bursts of activity of 15- to 70-ms duration, followed by a 300- to 700-ms period of suppression (36). Experimental evidence suggests that the timescales of interactions between LC and hippocampus (~1–2 s) (37) are compatible with the scale of occurrence of individual ripple episodes. Although the hypothesis that differentiated SPW-R complexes emerge partly as a result of LC inputs remains to be tested using more direct methods, it has been shown that decision making under uncertainty involves LC (38). Moreover, SPW-Rs are more frequent after task modifications, such as exposing an animal to a second novel environment (18).

In addition, nonclassical SPW-R subtypes may mark a differentiated involvement of the ascending serotonergic system. Notably, raphe projects to several subtypes of hippocampal GABAergic interneurons and may exert control on the *E–I* balance over local circuitry engaged during ripples via fast synapses (39). Moreover, the capacity of raphe projections to selectively influence well-segregated groups of hippocampal parvalbumin (PV) expressing interneurons has been recently stressed (40), raising the possibility of serotonergic control of neuronal circuits over timescales spanning the occurrence of single ripples (~200 ms). This view is further supported by a recent study where groups of the three major PV cell classes are differentially modulated during ripples, suggesting that fast network episodes involve distinct inhibitory circuits (41), modulated at timescales at which raphe–hippocampal modulations may occur.

Hippocampal–Neocortical Interactions May Contribute to SPW-R Variability. We showed that SPW-R subtypes 1 and 4 (nonclassical SPW-Rs) in the hippocampus consistently led to lesser activation across different cortical domains compared with SPW-R subtypes 2 and 3 (classical SPW-Rs). Because our experiments were performed in anesthetized macaque monkeys without any previous behavioral training, the robustness of our results across sessions suggests that these differentiated signatures reflect different types of brain-wide dynamical processes involving memory traces, not necessarily accounting for differences in memory content per se.

Differentiated activations were detected in the posterior and anterior cingulate (PCC, ACC) (42), PFC (43), and parietal cortices (44). One possible explanation for these results is that increased cortical activity marks enhanced recurrent interactions between neocortex and hippocampus during classical SPWs. Taking into account hippocampal connectivity, two recurrent mechanisms might account for differentiated SPW-R patterns. First, entorhinal cortex (EC) input may modulate CA1 activity by episodes of persistent activity that occur concomitantly with neocortical up-down state transitions (45). These neocortical–EC episodes develop at timescales similar to those of a typical burst of ripples, i.e., series of ripples with relatively short delays. Second, reentry may also be achieved at the scale of a single SPW-R event, through projections of medial entorhinal cortex (MEC) to CA1 stratum lacunosum moleculare (SLM) (46). Layer-specific activation of MEC would be followed by a local depolarization of SLM with the delay of a single synapse, thus influencing the time course of single SPW-Rs (46). In both scenarios, hippocampal activity could be controlled by recurrent activity within the local microcircuits and through cortico-hippocampal dialogue. These mechanisms might serve many purposes, such as volitional reactivation of a set of related memory traces or controlling the consolidation of new memories according to their relevance to preexisting memories and their reward value.

A Repertoire of Memory-Related Brain-Wide Events. To the best of our knowledge, the present study shows for the first time the existence of in vivo SPW-R subtypes occurring in the same recording site, and reflecting qualitative differences in brain activity within hippocampus and across cortical and subcortical domains. Processes such as memory reactivation, retrieval, and consolidation could exploit these brain-wide differences to fulfill different functions. Locally, the described SPW-R signatures may be the result of selective interactions between neuronal groups, involving varying degrees of network synchrony and dynamical *E–I* balance. This balance may be mediated by cortico-parahippocampal-hippocampal and subcortico-hippocampal interactions. Our results suggest these dynamical properties of local microcircuits are strongly intertwined with brain-wide interactions during SPW-R, possibly establishing distinct modes of selective processing and routing of information across multiple scales (*SI Section D*). The presented pattern classification will enable the characterization of SPW-Rs in behaving and natural sleep preparations and establish the functional role of each subtype. Finally, our approach could be used to better understand the underlying mechanisms of epileptiform events and more generally pathological phenomena (see ref. 47 for a perspective).

Materials and Methods

Surgical Procedures, Electrophysiology, and fMRI Recordings. Experimental and surgical procedures have been detailed in a previous study (27). In summary, a total of 242 experiments (10 min each) spread over 12 sessions were carried out in anesthetized male rhesus monkeys (*Macaca mulatta*). Head holders and recording chambers were located stereotaxically based on high-resolution anatomical MRI scans. Recordings were conducted in the anterior part of the hippocampus in the right hemisphere of each animal. All recording hardware, including the electrodes and amplifiers for simultaneous fMRI and multisite electrophysiological recordings, was developed at the Max Planck Institute for Biological Cybernetics. Custom-made, multicontact, NMR-compatible recording electrodes were made from a carbon fiber composite baton with 500-μm diameter (R&G). The 2.6-mm-long tip grounded down to a diameter of 250 μm. Electrodes contained 10 contacts

spaced 150 μm apart, with 6–10 targeting the structure of interest. Recording electrodes were positioned around the pyramidal layer of the hippocampal CA1 subfield (8–14 mm anterior of the interaural line). Fine adjustment of the recording electrode was achieved by intermediate MRI anatomical scans. Functional imaging was carried out in a vertical 4.7-T scanner with a 40-cm-diameter bore (BioSpec 47/40v; Bruker BioSpin), in which each animal was positioned in a custom-made chair [see Logothetis et al. (24) for details on the gradient coil]. Typically, 22 axial slices were acquired, covering the entire brain (voxel size, $0.75 \times 0.75 \times 2$ mm^3). BOLD activity was acquired at a resolution of 2 s with two-shot gradient-echo echo-planar imaging images (repetition time/echo time, 1,000/20 ms; bandwidth, 150 kHz; flip angle, 53°; field of view, 96×96 mm; matrix, 96×96; 2-mm slice thickness). MRI data were analyzed off-line. During all experiments, anesthesia was maintained with remifentanil (0.5–2 $\mu g \cdot kg^{-1} \cdot min^{-1}$) in combination with a fast-acting paralytic mivacurium chloride (5–7 $mg \cdot kg^{-1} \cdot h^{-1}$), known to only mildly affect the magnitude and time course of neural and vascular responses (24, 48). All experimental and surgical procedures were approved by the local authorities (Regierungspraesidium, Tübingen Referat 35, Veteriärwesen) and were in full compliance with the guidelines of the European Community (EUVD 86/609/EEC) for the care and use of laboratory animals.

Processing and Analysis of Neural Data. Analyses of electrophysiology and fMRI data were performed using MATLAB (The MathWorks). Signal denoising, electromagnetic interference elimination, and frequency band isolation procedures have been described in detail in a previous study (24). In *SI Section A*, we describe the main signal processing and neuronal data analysis performed on the denoised broadband extracellular signals (0.05 Hz to 7 kHz).

ACKNOWLEDGMENTS. We acknowledge A. Ramírez-Cárdenas and D. Zaldivar for insightful comments and discussions on previous versions of this manuscript. J. Werner and M. Schnabel provided excellent technical support during the development of this work. This research was supported by the Max Planck Society.

1. Euston DR, Tatsuno M, McNaughton BL (2007) Fast-forward playback of recent memory sequences in prefrontal cortex during sleep. *Science* 318(5853):1147–1150.
2. Johnson LA, Euston DR, Tatsuno M, McNaughton BL (2010) Stored-trace reactivation in rat prefrontal cortex is correlated with down-to-up state fluctuation density. *J Neurosci* 30(7):2650–2661.
3. Kudrimoti HS, Barnes CA, McNaughton BL (1999) Reactivation of hippocampal cell assemblies: Effects of behavioral state, experience, and EEG dynamics. *J Neurosci* 19(10):4090–4101.
4. Lee AK, Wilson MA (2002) Memory of sequential experience in the hippocampus during slow wave sleep. *Neuron* 36(6):1183–1194.
5. Nádasdy Z, Hirase H, Czurkó A, Csicsvari J, Buzsáki G (1999) Replay and time compression of recurring spike sequences in the hippocampus. *J Neurosci* 19(21): 9497–9507.
6. Skaggs WE, McNaughton BL (1996) Replay of neuronal firing sequences in rat hippocampus during sleep following spatial experience. *Science* 271(5257):1870–1873.
7. Wilson MA, McNaughton BL (1994) Reactivation of hippocampal ensemble memories during sleep. *Science* 265(5172):676–679.
8. Buzsáki G, Horváth Z, Urioste R, Hetke J, Wise K (1992) High-frequency network oscillation in the hippocampus. *Science* 256(5059):1025–1027.
9. Ylinen A, et al. (1995) Sharp wave-associated high-frequency oscillation (200 Hz) in the intact hippocampus: Network and intracellular mechanisms. *J Neurosci* 15(1 Pt 1): 30–46.
10. Ego-Stengel V, Wilson MA (2010) Disruption of ripple-associated hippocampal activity during rest impairs spatial learning in the rat. *Hippocampus* 20(1):1–10.
11. Gerrard JL, Burke SN, McNaughton BL, Barnes CA (2008) Sequence reactivation in the hippocampus is impaired in aged rats. *J Neurosci* 28(31):7883–7890.
12. Girardeau G, Benchenane K, Wiener SI, Buzsáki G, Zugaro MB (2009) Selective suppression of hippocampal ripples impairs spatial memory. *Nat Neurosci* 12(10): 1222–1223.
13. Nakashiba T, Buhl DL, McHugh TJ, Tonegawa S (2009) Hippocampal CA3 output is crucial for ripple-associated reactivation and consolidation of memory. *Neuron* 62(6): 781–787.
14. Karlócai MR, et al. (2014) Physiological sharp wave-ripples and interictal events in vitro: What's the difference? *Brain* 137(Pt 2):463–485.
15. Foster DJ, Wilson MA (2006) Reverse replay of behavioural sequences in hippocampal place cells during the awake state. *Nature* 440(7084):680–683.
16. Singer AC, Carr MF, Karlsson MP, Frank LM (2013) Hippocampal SWR activity predicts correct decisions during the initial learning of an alternation task. *Neuron* 77(6): 1163–1173.
17. Dupret D, O'Neill J, Pleydell-Bouverie B, Csicsvari J (2010) The reorganization and reactivation of hippocampal maps predict spatial memory performance. *Nat Neurosci* 13(8):995–1002.
18. Karlsson MP, Frank LM (2009) Awake replay of remote experiences in the hippocampus. *Nat Neurosci* 12(7):913–918.
19. Jadhav SP, Kemere C, German PW, Frank LM (2012) Awake hippocampal sharp-wave ripples support spatial memory. *Science* 336(6087):1454–1458.
20. Muenzinger KF (1938) Vicarious trial and error at a point of choice: I. A general survey of its relation to learning efficiency. *Pedagog Semin J Genet Psychol* 53(1):75–86.
21. Carr MF, Jadhav SP, Frank LM (2011) Hippocampal replay in the awake state: A potential substrate for memory consolidation and retrieval. *Nat Neurosci* 14(2):147–153.
22. Skaggs WE, et al. (2007) EEG sharp waves and sparse ensemble unit activity in the macaque hippocampus. *J Neurophysiol* 98(2):898–910.
23. Bland BH, et al. (2003) Effect of halothane on type 2 immobility-related hippocampal theta field activity and theta-on/theta-off cell discharges. *Hippocampus* 13(1):38–47.
24. Logothetis NK, et al. (2012) Hippocampal–cortical interaction during periods of subcortical silence. *Nature* 491(7425):547–553.
25. Fritzke B (1995) A growing neural gas network learns topologies. *Adv Neural Inf Process Syst* 7:625–632.
26. Shi J, Malik J (2000) Normalized cuts and image segmentation. *IEEE Trans Pattern Anal Mach Intell* 22(8):888–905.
27. Csicsvari J, Hirase H, Mamiya A, Buzsáki G (2000) Ensemble patterns of hippocampal CA3-CA1 neurons during sharp wave–associated population events. *Neuron* 28(2): 585–594.
28. Patel J, Schomburg EW, Berényi A, Fujisawa S, Buzsáki G (2013) Local generation and propagation of ripples along the septotemporal axis of the hippocampus. *J Neurosci* 33(43):17029–17041.
29. Ji D, Wilson MA (2007) Coordinated memory replay in the visual cortex and hippocampus during sleep. *Nat Neurosci* 10(1):100–107.
30. van der Meer MA, Redish AD (2009) Low and high gamma oscillations in rat ventral striatum have distinct relationships to behavior, reward, and spiking activity on a learned spatial decision task. *Front Integr Neurosci* 3:9.
31. Carr MF, Karlsson MP, Frank LM (2012) Transient slow gamma synchrony underlies hippocampal memory replay. *Neuron* 75(4):700–713.
32. Hofer KT, et al. (2015) The hippocampal CA3 region can generate two distinct types of sharp wave-ripple complexes, in vitro: Hippocampal sharp-waves in vitro. *Hippocampus* 25(2):169–186.
33. Reichinnek S, Künsting T, Draguhn A, Both M (2010) Field potential signature of distinct multicellular activity patterns in the mouse hippocampus. *J Neurosci* 30(46): 15441–15449.
34. Mizuseki K, Diba K, Pastalkova E, Buzsáki G (2011) Hippocampal CA1 pyramidal cells form functionally distinct sublayers. *Nat Neurosci* 14(9):1174–1181.
35. Aston-Jones G, Bloom FE (1981) Activity of norepinephrine-containing locus coeruleus neurons in behaving rats anticipates fluctuations in the sleep-waking cycle. *J Neurosci* 1(8):876–886.
36. Aston-Jones G, Cohen JD (2005) An integrative theory of locus coeruleus-norepinephrine function: Adaptive gain and optimal performance. *Annu Rev Neurosci* 28(1): 403–450.
37. Yavich L, Jäkälä P, Tanila H (2005) Noradrenaline overflow in mouse dentate gyrus following locus coeruleus and natural stimulation: Real-time monitoring by in vivo voltammetry. *J Neurochem* 95(3):641–650.
38. Payzan-LeNestour E, Dunne S, Bossaerts P, O'Doherty JP (2013) The neural representation of unexpected uncertainty during value-based decision making. *Neuron* 79(1):191–201.
39. Freund TF, Gulyás AI, Acsády L, Görcs T, Tóth K (1990) Serotonergic control of the hippocampus via local inhibitory interneurons. *Proc Natl Acad Sci USA* 87(21): 8501–8505.
40. Varga V, et al. (2009) Fast synaptic subcortical control of hippocampal circuits. *Science* 326(5951):449–453.
41. Varga C, et al. (2014) Functional fission of parvalbumin interneuron classes during fast network events. *Elife* 3:e04006.
42. Maddock RJ, Garrett AS, Buonocore MH (2001) Remembering familiar people: The posterior cingulate cortex and autobiographical memory retrieval. *Neuroscience* 104(3):667–676.
43. Wierzynski CM, Lubenov EV, Gu M, Siapas AG (2009) State-dependent spike-timing relationships between hippocampal and prefrontal circuits during sleep. *Neuron* 61(4):587–596.
44. Salazar RF, Dotson NM, Bressler SL, Gray CM (2012) Content-specific fronto-parietal synchronization during visual working memory. *Science* 338(6110):1097–1100.
45. Isomura Y, et al. (2006) Integration and segregation of activity in entorhinal-hippocampal subregions by neocortical slow oscillations. *Neuron* 52(5):871–882.
46. Kloosterman F, van Haeften T, Lopes da Silva FH (2004) Two reentrant pathways in the hippocampal-entorhinal system. *Hippocampus* 14(8):1026–1039.
47. Kerber K, et al. (2014) Differentiation of specific ripple patterns helps to identify epileptogenic areas for surgical procedures. *Clin Neurophysiol* 125(7):1339–1345.
48. Goense JBM, Logothetis NK (2008) Neurophysiology of the BOLD fMRI signal in awake monkeys. *Curr Biol* 18(9):631–640.
49. Saleem KS, Logothetis NK (2007) *A Combined MRI and Histology Atlas of the Rhesus Monkey Brain in Stereotaxic Coordinates* (Academic, London).
50. Łęski S, et al. (2011) Inverse current source density method in two dimensions: Inferring neural activation from multielectrode recordings. *Neuroinformatics* 9(4): 401–425.
51. Kortelainen J, Väyrynen E, Seppänen T (2011) Depth of anesthesia during multidrug infusion: Separating the effects of propofol and remifentanil using the spectral features of EEG. *IEEE Trans Biomed Eng* 58(5):1216–1223.
52. Battaglia FP, Sutherland GR, McNaughton BL (2004) Hippocampal sharp wave bursts coincide with neocortical "up-state" transitions. *Learn Mem* 11(6):697–704.
53. Seber GAF, Wild CJ (1989) Computational methods for nonlinear least squares. *Nonlinear Regression* (Wiley, Hoboken, NJ), pp 619–660.

54. Fritzke B (1994) Growing cell structures—a self-organizing network for unsupervised and supervised learning. *Neural Netw* 7(9):1441–1460.
55. Martinetz TM, Berkovich SG, Schulten KJ (1993) Neural-gas' network for vector quantization and its application to time-series prediction. *IEEE Trans Neural Netw* 4(4):558–569.
56. Yu SX, Shi J (2003) Multiclass spectral clustering. *Proceedings of the Ninth IEEE International Conference on Computer Vision* (IEEE, Washington, DC), pp 313–319.
57. Smola AJ, Kondor R (2003) Kernels and regularization on graphs. *Learning Theory and Kernel Machines,* Lecture Notes in Computer Science, eds Schölkopf B, Warmuth MK (Springer, Berlin), Vol 2777, pp 144–158.
58. Desgraupes B (2013) *Clustering Indices*. Available at https://cran.r-project.org/web/packages/clusterCrit/vignettes/clusterCrit.pdf. Accessed February 17, 2014.
59. Bokil H, Andrews P, Kulkarni JE, Mehta S, Mitra PP (2010) Chronux: A platform for analyzing neural signals. *J Neurosci Methods* 192(1):146–151.
60. Hájos N, et al. (2013) Input-output features of anatomically identified CA3 neurons during hippocampal sharp wave/ripple oscillation in vitro. *J Neurosci* 33(28):11677–11691.
61. Sullivan D, et al. (2011) Relationships between hippocampal sharp waves, ripples, and fast gamma oscillation: Influence of dentate and entorhinal cortical activity. *J Neurosci* 31(23):8605–8616.
62. Buzsáki G, et al. (2003) Hippocampal network patterns of activity in the mouse. *Neuroscience* 116(1):201–211.
63. Schölkopf B, Smola AJ (2001) *Learning with Kernels: Support Vector Machines, Regularization, Optimization, and Beyond* (MIT, Cambridge, MA).
64. Lee S-H, et al. (2014) Parvalbumin-positive basket cells differentiate among hippocampal pyramidal cells. *Neuron* 82(5):1129–1144.
65. Sørensen JC, Tønder N, Slomianka L (1993) Zinc-positive afferents to the rat septum originate from distinct subpopulations of zinc-containing neurons in the hippocampal areas and layers. A combined fluoro-gold tracing and histochemical study. *Anat Embryol (Berl)* 188(2):107–115.